Hydrogen-related complexes as the stressing species in high-fluence, hydrogen-implanted, single-crystal silicon

G. F. Cerofolini and L. Meda

Functional Materials Laboratory, Istituto Guido Donegani, EniChem, 20097 San Donato MI, Italy

R. Balboni, F. Corni, S. Frabboni, G. Ottaviani, and R. Tonini

Dipartimento di Fisica, Università di Modena, 41100 Modena MO, Italy

M. Anderle and R. Canteri

IRST—Divisione di Scienza dei Materiali, 38050 Povo TN, Italy

This work is devoted to the characterization of the Si:H system obtained by high-fluence, low-energy, hydrogen implantation into single-crystal silicon. The implanted hydrogen profile and the ones resulting after thermal annealing in the range 100–800 °C are detected by secondary-ion mass spectrometry and elastic-recoil detection analysis. The displacement field in the crystal, measured by channeling Rutherford-backscattering spectrometry, is found to depend on the direct radiation damage, the extended defects formed after ion implantation (revealed by transmission electron microscopy), and the implanted species. The contribution to the displacement field due to hydrogen-related defects has a characteristic "reverse annealing" in the range 100–400 °C, essentially due to their formation kinetics.

I. INTRODUCTION

Though "none of the numerous hydrogen-related vibration bonds have yet been assigned to a specific defect",[1] there is now a reasonable consensus on hydrogen configurations in single-crystal silicon at *low concentration*.

(1) The bond-centered (BC) configuration, typical of intrinsic or *p*-type silicon [Fig. 1(a) and Refs. 2 and 3].

(2) The antibonding (AB) configuration, where hydrogen is kept close to an interstitial tetrahedral (T_d) position by an antibonding state of silicon [Fig. 1(b) and Ref. 4].

(3) The H_2^* configuration, resulting from pairing of close, ionized, AB (H^-) and BC (H^+) hydrogen atoms [Fig. 1(c) and Ref. 3].

(4) The silanic Si-H configuration, resulting from hydrogen reaction with a silicon dangling bond [Fig. 1(d)].

The standard theory of shallow dopants ascribes acceptor passivation to a positively ionized BC hydrogen in the vicinity of a negatively ionized acceptor [Fig. 2(a) and Ref. 3]; the deep-dopant description ascribes passivation to the formation of a silanic bond in the vicinity of an sp^2-hybridized acceptor [Fig. 2(b) and Ref. 5].

Much more complex is the situation at *high concentration*, where unsaturated or ionized hydrogen configurations (AB, BC, or H_2^*) are expected to rearrange and form saturated configurations (e.g., molecular hydrogen, H_2), this process being counterbalanced by steric factors that make the incorporation of the molecules in the lattice difficult.

The existence of H_2 in crystalline silicon is highly controversial: Quantum calculations show that H_2 in an interstitial T_d site oriented in a $\langle 100 \rangle$ direction is one of the most stable compounds in silicon and is therefore expected to be one preferred configuration of high concentration in crystalline, nondefective silicon;[6,7] however, no direct spectroscopic evidence for H_2 has yet been presented. On the experimental side, H_2 has been advocated in
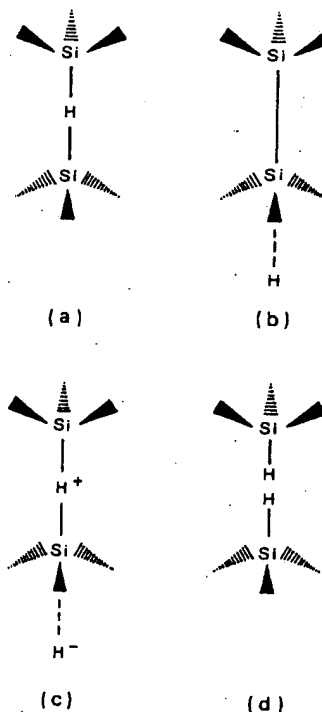

FIG. 1. Suggested hydrogen configuration in silicon: (a) bond-centered, (b) antibonding, (c) H_2^*, and (d) silanic.
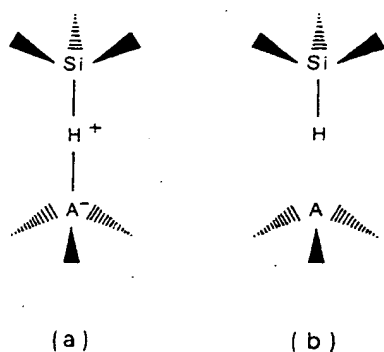
FIG. 2. Suggested mechanisms of acceptor passivation in (a) the standard theory of shallow dopants (by a positively charged, bond-centered hydrogen), and (b) the deep-dopant description of an acceptor (by a silanic bond with an unsaturated silicon atom).

many cases: Hall has explained experimental diffusion profiles in terms of coexisting H and H_2 in local thermodynamic equilibrium;[8] Cerofolini and Ottaviani, in order to explain their channeling Rutherford-backscattering-spectrometry (RBS) data, have assumed that atomic hydrogen, remaining in the crystal after low-temperature (77 K) ion implantation, reverts to H_2 after annealing at moderate temperature (400–450 °C);[9] Stutzmann *et al.*, basing their arguments on infrared and effusion data, reach the conclusion that H_2 is formed in annealed *p*-type silicon;[10] but Boyce remarks that H_2 has been detected only in microcrystalline silicon, where it can be embedded in microcavities among microcrystals.[11]

Together with these pointlike defects, extended defects involving hydrogen have also been reported: namely {100} and {111} platelets[12–15] and bubbles.[16]

To deepen our knowledge of the state of high-concentration hydrogen in silicon, we have hence undertaken an extended experimental characterization of single-crystal silicon implanted at high fluence (1.6×10^{16} cm^{-2}) and low energy (15.5 keV) at room or liquid-nitrogen temperature with the goal of verifying under which annealing conditions the implanted hydrogen is able to produce a displacement field in the crystal. The techniques used in the present characterization are secondary-ion-mass spectroscopy (SIMS), channeling RBS, elastic-recoil detection analysis (ERDA), and conventional and high-resolution transmission electron microscopy (TEM and HREM).

II. EXPERIMENT

The complete experimental setup of our collaboration is described in Ref. 17. The major difference with respect to that work is that all the implantations have been carried out taking care not to produce any appreciable target heating.

A. Sample preparation

Samples were prepared by implanting H_2^+ into single-crystal silicon. The silicon slices were 6 in. in diameter,

Czochralski grown, (100) oriented, and *p* type, with a resistivity in the interval 30–50 Ω cm (the corresponding dopant concentration is much lower than hydrogen concentration, so the sample can be considered intrinsic). The implantations were carried out by tilting the slices by 7° with respect to the beam.

Samples were implanted with H_2^+ at an energy of 31 keV. Because of the H_2^+ fragmentation at the surface and low density of the collisional cascades, this implantation is equivalent to the implantation of atomic hydrogen at double fluence and an energy of 15.5 keV. Data will henceforth be presented in terms of atomic energy E and fluence Φ.

The implantations were carried out either at approximately 300 K (in an Eaton Nova 10/160 ion implanter, operated at a beam-current density for which there is no appreciable sample heating), or at approximately 77 K (in a Varian ion implanter operated at very low current density, ≈ 1 μA/cm^2, with an end station modified to allow the target to be cooled by a good thermal contact with a liquid-nitrogen heat sink).

Annealing experiments were carried out by heating the samples in a vacuum in the temperature interval 100–800 °C.

B. Measurements

Secondary-ion mass spectrometry. Depth profiles of sputtered negative ions with masses of 1 amu were determined by using a CAMECA IMS-4f ion microprobe, with Cs$^+$ as the primary ion at an energy of 14.5 keV, and a sample-chamber vacuum of about 5×10^{-7} Pa. The primary current density was adjusted to obtain a high sputtering rate (≈ 3 nm/s) stable during the measurement to within 0.5%. These conditions allow us to reduce typical problems of hydrogen depth profiling, mainly related to the contamination of the sample chamber. Knock-on artifacts affect the hydrogen profiles particularly in the distributions wings, where the hydrogen concentration is lower than 2×10^{18} cm^{-3}. This effect is responsible for an uncertainty in the depth scale smaller than the depth resolution ($\lesssim 10$ nm) and for a background level increase. To avoid the characterization of artifacts and of diffused profiles, we limit our considerations around the maxima of the distributions.

Elastic-recoil detection analysis. Forward scatterings were performed by using a 2.3-MeV He$^+$ beam (with a section of 0.1×3 mm^2) impinging the sample at a glancing angle of 75° from the sample normal. The detector, placed 150° from the beam direction and 15 cm from the sample, was covered with a collimator 2 mm wide and 5 mm long. The forward-scattered helium particles were stopped by a 10-μm-thick Mylar film. These data were used to follow the hydrogen evolution after annealing in the concentration region just above 10^{20} cm^{-3}. Comparative measurements produced coincident SIMS and ERDA profiles within experimental uncertainties.

Channeling Rutherford-backscattering spectrometry. Channeling RBS analyses were performed by using a 2-MeV facility; the RBS spectra were obtained by impinging a 1-MeV He$^+$ beam into implanted samples, with a

TABLE I. Average diameter $(\bar{d})$ and total number (n_{TEM}) of extended defects, number of atoms arranged in extended defects (N_{TEM}), and number of displaced silicon atoms as determined from channeling RBS (N_{RBS}).

	As-implanted	400 °C	Sample annealed at 600 °C	800 °C
$\bar{d}$ (nm)	7 ± 2	12 ± 3	30 ± 3	40 ± 4
n_{TEM} (cm^{-2})	$(9\pm2)\times10^{11}$	$(5\pm1)\times10^{11}$	$(1.2\pm0.1)\times10^{11}$	$(2.1\pm0.1)\times10^{10}$
N_{TEM} (cm^{-2})[a]	$(4\pm3)\times10^{14}$	$(7\pm5)\times10^{14}$	$(1.1\pm0.3)\times10^{15}$	$(3.4\pm0.8)\times10^{14}$
N_{RBS} (cm^{-2})[b]	3×10^{16}	6×10^{16}	4×10^{16}	7×10^{15}

[a]The silicon density in defects was assumed to be 10 nm^{-2}.
[b]The estimated uncertainty is $\pm10\%$.

scattering angle of 130° and an integrated charge in the range 30–100 μC. Spectra were compared with those obtained from an undamaged reference sample both in channeling and in random conditions. Details describing how the distribution of displaced atoms is extracted from a channeling RBS spectrum are given in the Appendix.

Electron microscopy. Transmission-electron-microscopy observations concerning density, distribution, and location of extended defects were carried out with a Philips EM 400 ST electron microscope; high-resolution investigations of their structures were carried out with a JEOL 2010 electron microscope (point resolution 0.23 nm).

III. EXPERIMENTAL RESULTS

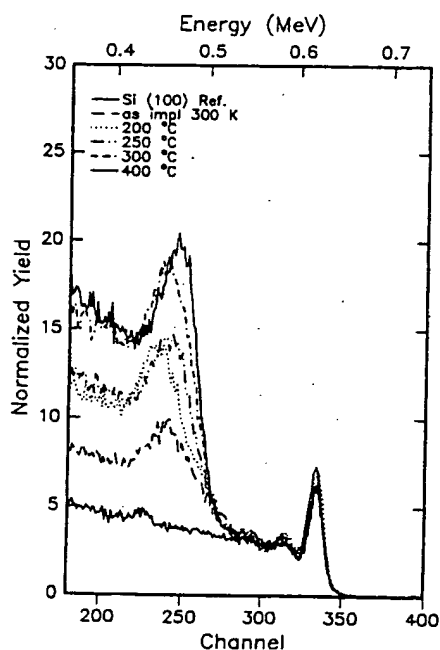The results of interest are summarized in Figs. 3–8 and in Table I.

FIG. 3. Channeling RBS spectra of the samples implanted at 300 K and annealed for 2 h in the temperature range 200–400 °C.

A. Formation of a displacement field

Annealing in the range 200–400 °C induces the formation of a strong displacement field (detected by RBS), quite irrespective of the target temperature during the implantation. Figure 3 shows the RBS spectra after isochronal (2 h) annealing of samples implanted at 300 K; no appreciable difference (apart from the as-implanted spectrum[9]) was detected in the samples implanted at 77 K. Figure 4 shows the kinetics of the formation of a displacement field in isothermal conditions ($T=200$ °C), showing that this phenomenon is not saturated after 2 h of annealing. (In Ref. 18 it was tacitly assumed that the displacement field increases linearly with time; actually, Fig. 4 shows a complex behavior that makes the conclusions reached therein concerning the activation energy of the process questionable.)

Rutherford-backscattering dechanneling measurements (carried out at different beam energies) in samples annealed in the interval 450–500 °C for 2 h show that the scattering centers are uncorrelated and their total amount per unit area is approximately 10^{18} cm^{-2}, irrespective of target temperature (77 or 300 K) during implantation.
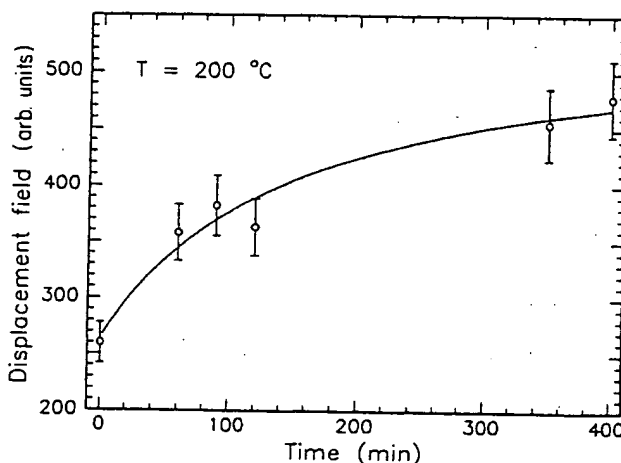

FIG. 4. Kinetics of displacement-field formation (integral of the displacement field vs annealing time). The line has been drawn only to guide the eyes.

B. Hydrogen effusion and destruction
of the displacement field

While heat treatments at $T < 400\,°C$ do not produce appreciable hydrogen out-diffusion, heat treatments at $T \gtrsim 400\,°C$ produce a fast hydrogen loss, terminating at a saturation value. This conclusion follows from the kinetics of hydrogen loss determined by ERDA (Fig. 5). As hydrogen is gradually lost, the displacement field is progressively reduced as shown by RBS (Fig. 6). Once the displacement field has reached its maximum value (around $400\,°C$), heat treatments at higher temperature simultaneously produce a loss of hydrogen and a reduction of the displacement field. The displacement field decreases with T approximately like the amount of hydrogen, thus suggesting that they are strictly correlated.

The kinetics of hydrogen loss are associated with two regimes: the initial regime is characterized by a fast hydrogen loss; the steady-state regime is characterized by a hydrogen concentration almost independent of the annealing duration. Interpreting this quasi-steady-state as an equilibrium, an effusion pseudoenthalpy ΔH_{eff} can be determined by an Arrhenius plot of experimental data; this plot gives $\Delta H_{eff} = 0.25 - 0.30$ eV.

C. Extended defects

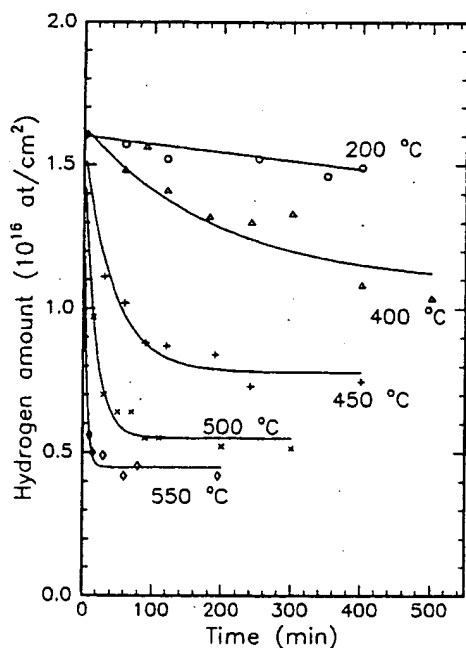Electron microscopy shows the presence of a heavily damaged region with depth between approximately 160

FIG. 6. Channeling RBS spectra of the samples implanted at 300 K and annealed for 2 h in the temperature range 400–800 °C.

FIG. 5. Hydrogen effusion kinetics (amount of hydrogen, Q_H, vs annealing time t) in the temperature range 400–550 °C. The experimental data have been fitted by the equation $Q_H(t) = Q_H(0)\exp(-t/\tau) + Q_H^{SS}$, where τ is the lifetime of the effusion kinetics and Q_H^{SS} is the steady-state value.
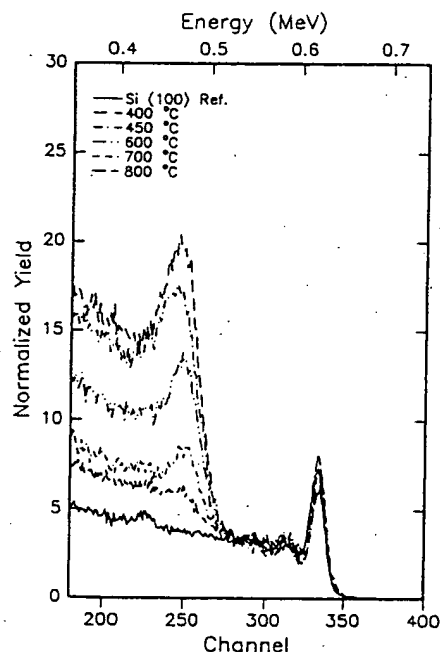
and 260 nm, where RBS detects the presence of a strong displacement field both in as-implanted samples and in samples annealed at 400 °C.

The extended defects detected in the implanted samples are $\{100\}$ and $\{111\}$ platelets, often observed in high-fluence hydrogen implantation,[15] and $\{113\}$ platelets, usually detected in silicon-implanted layers.[19] Figure 7 shows HREM pictures of (a) a $\{100\}$ platelet, (b) a $\{111\}$ platelet, and (c) a $\{113\}$ platelet. Through-focal observations in the diffraction-contrast mode have shown a behavior characteristic of zones with a density lower than that of the host matrix, therefore suggesting a possible hydrogen content.

The shape and size of the hydrogen-related platelets vary with annealing temperature, ranging from a diameter of about 7 nm in as-implanted samples (300 K) to an average diameter of approximately 12 nm after annealing at 400 °C. Annealing at higher temperature produces different defects: extrinsic defects with size increasing from 30 to 40 nm as T increases from 600 to 800 °C, and three-dimensional defects, with lower electro-optical density, whose evolution in shape and size is understood by comparing the pictures shown in Fig. 8.

Also, the in-depth distribution of extended defects varies with annealing temperature: it is almost uniform in the region $160 < x < 260$ nm in the samples heated up to 600 °C, and extends approximately over the same region, but is bell shaped with a maximum at 190 nm in the samples heated at 800 °C. Table I reports the most important quantitative features of the defects observed in the considered samples.
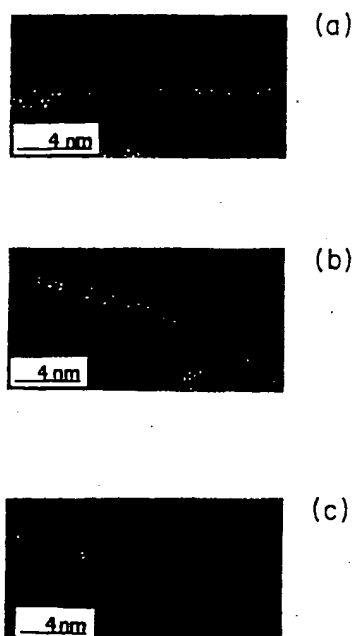
FIG. 7. High-resolution electron micrographs of (a) a {100} platelet, (b) a {111} platelet, and (c) a {113} platelet.

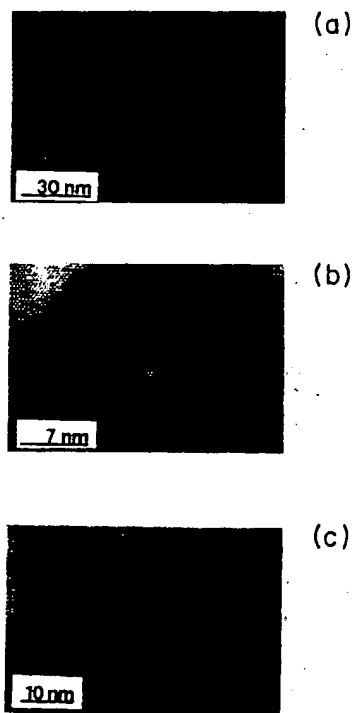FIG. 8. (a) Near-⟨100⟩-projection plan view of a defective region in a sample annealed at 600 °C for 2 h. Through focal observations in the diffraction-contrast mode have shown that the particles are less dense than the matrix. (b) HREM image of typical defects observed in samples annealed at 600 °C. (c) Near-⟨110⟩-projection cross-sectional view of defects observed in samples annealed at 800 °C. Comparison of (b) and (c) suggests that the defect-growth mechanism is Ostwald ripening.

Taking into account that (1) the energy behavior of dechanneling suggests that the scattering centers are not correlated, (2) the amount of silicon atoms in extended defects and the distortion field they produce increase monotonically with T up to 600 °C, while the number of displaced atoms has a maximum of 400 °C; and (3) for all T ($T \lesssim 600$ °C) the in-depth distribution of atoms in extended defects is almost uniform in the range 160–260 nm, while the distributions of displaced atoms are quite sharp and centered on somewhat different depths at different temperatures, it may reasonably be argued that the extended defects detected by electron microscopy play a small effect on the displacement field detected by RBS.

IV. SOURCES OF THE DISPLACEMENT FIELD

Since thermal treatments in the range 200–400 °C induce the formation of a strong displacement field (Fig. 3) while the hydrogen profile remains substantially unchanged, we are forced to ascribe the displacement field to some hydrogen-related complexes whose nature changes with the annealing conditions rather than to hydrogen itself. Two kinds of hydrogen-related complexes are identified as sources of displacement fields: one (referred to as H_*) responsible for a weak displacement field, formed in the defect-free wing of the distribution (centered on a depth of about 230 nm), and disappearing after annealing at $T > 200$ °C; and the other (referred to as H_{**}) responsible for a strong displacement field, formed in the defective region of maximum hydrogen concentration after heat treatments at $T > 200$ °C, and stable up to at least 600 °C.

The existence of two hydrogen-related stressing species with different thermal behaviors was identified in previous works of this collaboration.[20] However, due to inherent difficulties in the quantitative analysis of the RBS spectrum, the RBS data were treated in a semiquantitative manner. Consequently, our preliminary analyses may have led to erroneous conclusions.

In this work we deepen our study by means of the new method for the analysis of the channeling RBS spectrum described in the Appendix. The analysis of the RBS spectra shown in Figs. 3 and 6 is the point of origin of the distributions of displaced atoms reported in Figs. 9 and 10, respectively. The interpretation of these distributions in terms of a hydrogen-induced displacement field is not straightforward and requires that the total displaced atoms are subtracted by the sum of the displaced atoms associated with extended defects and the self-interstitials produced by the implantation itself.

First of all, we recall that most of the phenomenology observed by RBS is not due to extended defects. Indeed, the correlation of the scattering centers (uncorrelated versus correlated), the annealing behavior (the RBS signal is at a maximum at 400 °C, while extended defects increase monotonically up to 600 °C), and the form of the distribution (centered on a depth between 200 and 250 nm according to T with a full width at half-height of 50 nm versus a uniform distribution in the range 160–260 nm) give evidence that extended defects bring a small (but

not negligible) contribution to the displacement field detected by RBS. However, since in the sample annealed at 800 °C hydrogen is no longer present and the in-depth distribution of the displaced atoms detected by channeling RBS is the same as the in-depth distribution of extended defects detected by TEM, it may reasonably be argued that in this situation all the displaced atoms are due to extended defects. This argument leads to the conclusion that each atom in the extended defect is responsible for approximately 20 equivalent RBS-active atoms (see Table I). In all other situations in which hydrogen is present the in-depth distribution of displaced atoms produced by extended defects is assumed to be the same (flat up to 600 °C and bell shaped at 800 °C) as determined by TEM analysis multiplied by the above factor 20.

The self-interstitial distribution can be calculated by existing simulators (in our case, TRIM, denoting "transport of ions in matter"[21]) by adjusting the electronic stopping (by approximately 10%) to match the experimental hydrogen distribution and the threshold displacement energy to match the displaced-atom distribution in the region where the effect of the implanted impurity is negligible (in our case, in the depth region $x \lesssim 120$ nm where neither H_a nor H_{aa} are present).

The analysis of the RBS spectra of the samples implanted at 300 K in the depth region $x \lesssim 120$ nm suggests that the as-implanted self-interstitial distribution is unchanged after annealing at $T \lesssim 300$ °C and is appreciably annealed out for $T \gtrsim 400$ °C. This conclusion is consistent with the thermodynamic analysis of Roorda *et al.* showing that the recovery of crystalline silicon damaged by the implantation of *high-energy*, light ions takes place quite uniformly in the temperature range 100–400 °C, the

released energy being approximately 1 eV per displaced atom.[22] This value results from the weighted average of the energy excess stored in Frenkel pairs [tentatively, in the range 4–8 eV/pair (Ref. 23)], amorphous islands formed by high-energy silicon recoils[24] [approximately 0.13 eV/atom (Ref. 25)], or agglomerates of point defects (e.g., divacancies[26]). Since the recovery kinetics of separated amorphous islands, formed by arsenic implantation (the ion for which data are available with the closest mass to that of silicon,[27] is in the range 100–150 °C, while divacancies anneal out around 200 °C,[26] the following attribution seems realistic:

(a) 100–150 °C, temperature range for the annealing of amorphous islands.

(b) 150–250 °C, temperature range for the annealing of divacancies.

(c) 250–400 °C, temperature range for the annealing of self-interstitials.

Remembering that in our experiment the implantation energy was not sufficient to form amorphous islands and that divacancies are, to the first order, RBS-inactive, it may reasonably be argued that the RBS signal due to self-interstitials disappears in the temperature range 250–400 °C, in substantial agreement with our finding. It is also possible that in our case the system is partially protected against Frenkel-pair recombination by vacancy or interstitial reaction with the atomic hydrogen.

Subtracting the remaining interstitials and the displacement field due to extended defects from the total displaced atoms, the hydrogen-induced distributions are eventually obtained. An example showing the various
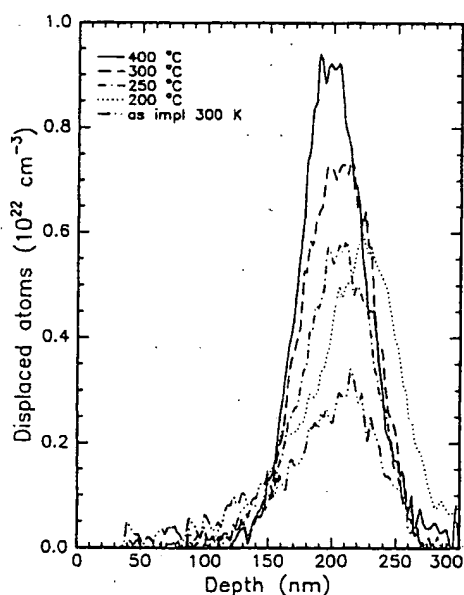
FIG. 9. In-depth distributions of displaced atoms of samples annealed at a temperature below 400 °C for 2 h; heating at 350 °C produces the same displaced-atom distribution as heating at 400 °C.
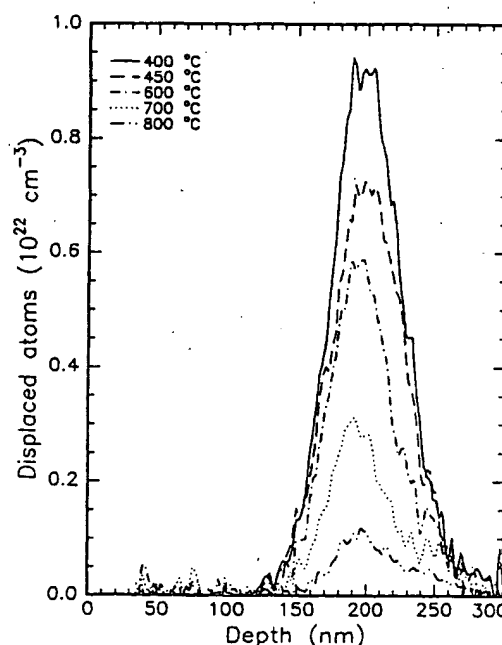
FIG. 10. In-depth distributions of displaced atoms of samples annealed in the temperature range 400–800 °C for 2 h.
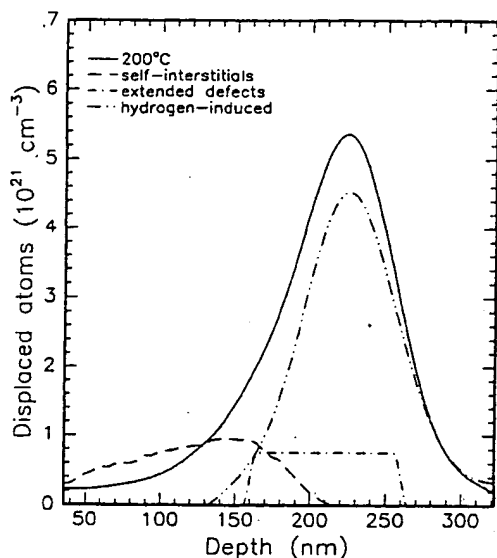
FIG. 11. Separation of the various contributions (hydrogen induced, or due to self-interstitials or extended defects) to the displacement field in the sample annealed at 200 °C.

contributions to the experimental displacement field in the sample annealed at 200 °C is shown in Fig. 11.

The above analysis confirms the original qualitative conclusion relating the displacement field to hydrogen-related complexes: A displacement field is already present in as-implanted conditions (300 K) in the bulk tail of the hydrogen distribution ($x \gtrsim 250$ nm) and remains unchanged after annealing at 150 °C; heating at a temper-
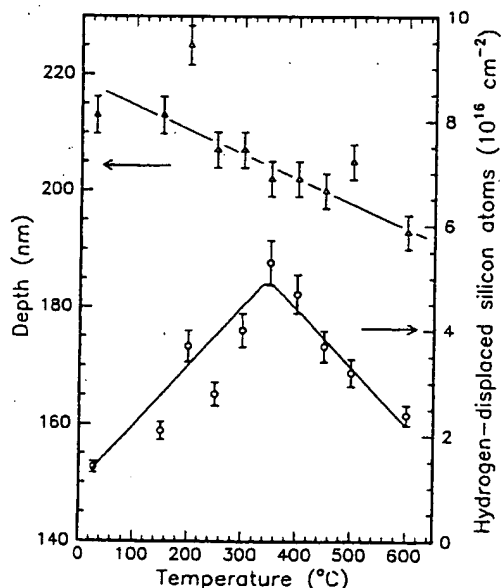

FIG. 12. Graphs showing the evolution vs annealing temperature of the amount of hydrogen-displaced silicon atoms and of their most probable depth. The lines have been drawn only to guide the eyes.

ature higher than 200 °C (but not greater than 400 °C) produces an increase in intensity and a gradual shift toward the surface of the displacement field; heating at higher temperature produces a gradual loss of hydrogen without further change of shape or depth distribution (Fig. 12).

V. STRUCTURE OF THE HYDROGEN-RELATED COMPLEXES

The analysis described in the preceding sections has led to the identification of two stressing species, referred to as H_* and H_{**}, irrespective of their actual chemical nature.

In view of its depth location and annealing behavior, the identification of H_* as molecular hydrogen, H_2, seems plausible; of course, this attribution has mainly a conventional character, and in the absence of direct spectroscopic evidence it must be considered a putative stipulation.

In this section we speculate on the nature of the H_{**} center. The driving force leading to the formation of the H_2 molecule starting from silanic, BC or AB configurations is the electronic energy gained in its synthesis (see, for instance, the estimate of Ref. 20), which greatly counterbalances the modest energy required to sustain the weak displacement field produced by the molecule.

What is obscure in this picture is which driving force is able to transform H_2 molecules, each producing a weak displacement field, in the complex H_{**}, which requires an appreciable energy to sustain the strong displacement field it originates. Molecular hydrogen in interstitial sites is, however, in a strained configuration, as confirmed by the calculation of its bond length (0.086 nm, 15% larger than in vacuum) and energy (approximately 2 eV, versus 4.75 eV of the free molecule).[6,7] An H_2 molecule in a vacancy or in larger voids is therefore expected to be more stable, and its formation is allowed because the energy required to dissociate two silanic bonds is counterbalanced by the molecule formation and the saturation of the resulting dangling bonds.[20] Since the H_{**} complex is formed in the zone of maximum hydrogen concentration, where intrinsic defects are presumably fully decorated, it is therefore not unrealistic to assume that H_{**} is formed by several H_2 molecules in defects of intrinsic nature, such as vacancies, divacancies, intrinsic stacking faults, etc.

The location of the H_{**} complex in the zone of maximum radiation damage, together with the fact that after annealing at $T > 400$ °C the displacement field decreases approximately in proportion to the total amount of hydrogen, might suggest that the H_{**} complex is stabilized by its interaction with silicon extended defects formed during annealing. The decorated defects so formed could eventually evolve to form the {100} and {111} platelets observed in Refs. 12 and 13 by transmission electron microscopy. Though this model is partially sustained by TEM evidence that {100}, {111}, and {113} defects obtained after annealing at 400 °C are less dense than bulk silicon (thus suggesting their possible decoration with hy-

drogen), it does not explain the RBS behavior for $T < 400\,°C$.

More plausible is the following mechanism, for which H_{**} is seen as a set of separated molecules fixed in preferential sites (vacancy clusters) by steric factors.

(1) In as-implanted conditions at 300 K, atomic hydrogen (in BC or interstitial positions) diffuses until it reacts with another hydrogen atom to form a hydrogen molecule,

$$H + H \rightarrow H_2 ,$$
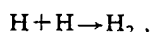
which rests in the position where it was formed. This process is expected to take place in the region where vacancies (v) either are not formed or are in insufficient concentration to bind hydrogen with silanic bonds and is completed at $T \lesssim 200\,°C$; this argument suggests that H_2 is formed starting from $x \gtrsim 200$ nm to a depth limited by atomic hydrogen diffusivity.

(2) Annealing at $T \gtrsim 200\,°C$ produces decomposition of silanic bonds[28] of fully decorated vacancies (denoted v-H_4) and the formation of the H_{**} complex,

$$(v - H_4)_{n/2} \rightarrow v_{n/2} + nH_2 ,$$
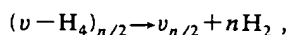
in the region where close, fully decorated vacancies are present (150–200 nm). The hydrogen-related defect so produced is formed by $n/2$ vacancies embedding n H_2 molecules ($H_{**} = v_{n/2} \cdots nH_2$) and is thought of as immobile because the close vacancies form a preferential site where hydrogen can stay.

This mechanism (which requires the existence of intrinsic defects, each bonding several hydrogen atoms, evidence of which has recently been given[29,30]) also explains why H_{**} is formed in the zone with simultaneously high hydrogen and vacancy concentrations.

The size of the hydrogen-related complex H_{**} can be estimated from RBS dechanneling data by assuming that after prolonged annealed at $T > 400\,°C$ practically all hydrogen is embedded in separated complexes and that each of them displaces approximately 10^3 atoms from their lattice positions (this estimate is taken from the thermodynamic analysis of Ref. 23, Chap. 7); this estimate gives that the H_{**} complex is formed by approximately four H_2 molecules (this gives a better specification of the nanocavity at 400 °C, $H_{**} = v_2 \cdots 4H_2$).

Assuming that each H_{**} complex is actually formed by n molecules in a supercompressed gas phase at a density of the order of $(0.5-1) \times 10^{23}$ cm^{-3} (corresponding to one to two H_2 molecules per vacancy), the pressure exerted by the gas on the silicon is of the order of 10^8 Pa and the corresponding lattice strain, $\simeq 10^{-3}$, is of the same order as that observed by this collaboration by multiple-crystal x-ray diffraction.[31]

The nanocavities in which the complexes H_{**} are embedded become closer and closer as fluence increases and eventually may coalesce to form voids containing hydrogen bubbles, as reported in the literature.[15,16] We have also been convinced of the formation of cavities by the observation of octahedral defects (which are the equilibrium shapes of cavities in silicon) after annealing at 800 °C

[see Fig. 8(c)].

This model also explains why the system prefers to arrange in a configuration of higher stress—indeed, the driving force is the energy gained in relaxing the H-H bond from a length of 0.086 nm (bond energy of $\simeq 2$ eV) in its interstitial position to a length of 0.074 nm (bond energy of 4.75 eV) in vacancies or larger cavities.

VI. CONCLUSIONS

A combined experimental analysis of the Si:H system obtained by high-fluence ion implantation in (100) single-crystal silicon at room or liquid-hydrogen temperature, based on channeling RBS, conventional and high-resolution TEM, ERDA, and SIMS profiling, has allowed us to identify the following important items.

(1) Two hydrogen-related complexes, H_* and H_{**} are the major sources of the displacement field in the crystal.

(2) H_* is observed in the defect-free wing of the hydrogen distribution in as-implanted samples and is destroyed by annealing at $T > 200\,°C$; this hydrogen-related center is attributed to isolated H_2 molecules.

(3) H_{**} is formed after annealing at $T > 200\,°C$ in the silicon region where radiation damage and hydrogen concentration are both high; this hydrogen-related center is stable up to at least 600 °C and is attributed to small bubbles of H_2 molecules.

APPENDIX: ANALYSIS OF RBS SPECTRA

In this appendix we shall assume that the energy axis of RBS spectra has already been transformed in a depth axis and that the backscattering yield Y as a function of depth x is experimentally known. Together with the function $Y(x)$ for the considered sample, two other RBS profiles are assumed known: $Y^{unimpl}(x)$, the RBS yield for an undamaged crystal, and $Y^{random}(x)$, for the randomly oriented (or amorphous) silicon.

Channeling RBS spectra are often used in a qualitative fashion, since their quantitative interpretation requires the exact specification of the lattice location of the backscattering centers[17] and a knowledge of how multiple scatterings, in turn responsible for dechanneling, affect the baseline. This last point is especially important in situations (like those considered in this work) in which two peaks of comparable intensities are suspected to be present and separated by a distance ($\simeq 40$ nm) just slightly higher than the depth resolution ($\simeq 20-30$ nm) of the RBS technique. The peaks in Figs. 3 and 6 indeed seem centered on different depths in samples annealed at different temperatures, but this conclusion might only be

apparent because the (unknown) baseline $B(x)$ affects the estimate of the direct backscattering yield $D(x)$ $[D(x)=Y(x)-B(x)]$. This effect is especially important in all cases (like ours) in which $B(x)$ is of the same order as $D(x)$.

We have hence undertaken the development of an *objective* method for constructing the baseline on serious physical bases; this method seems to us quite general.

The basic assumption upon which our method is constructed is the following:

(A) The concentration of backscattering centers is proportional to the concentration of dechanneling centers.

This hypothesis allows the baseline $B(x)$ to be constructed:

With reference to the ideal situation of Fig. 13 (which is representative of a wide class of actual cases), first of all identify the depth region (x_Q, x_P) in which scattering centers are present; in principle, x_Q can coincide with the surface. In the region (x_Q, x_P) the baseline increases gradually from $B(x)=Y^{\text{unimpl}}(x)$ for $x < x_Q$ to $B(x)=Y(x)$ for $x_P \leq x$. The analysis cannot proceed further without approximating the baseline in this region by means of an analytical function; a linear approximation, $B(x)=Y_P + m(x-x_P)$ [where m is the tangent to the experimental curve $Y(x)$ in a right neighbor of P], is particularly useful.

The gradual increase of the baseline in the interval (x_Q, x_P), physically due to the loss of collimation of the impinging beam as a greater and greater number of scattering centers are met, can be described by an equation such as

$$B(x)=[1-\lambda(x)]Y^{\text{unimpl}}(x)+\lambda(x)[Y_P + m(x-x_P)] \; .$$

$$(\text{A1})$$

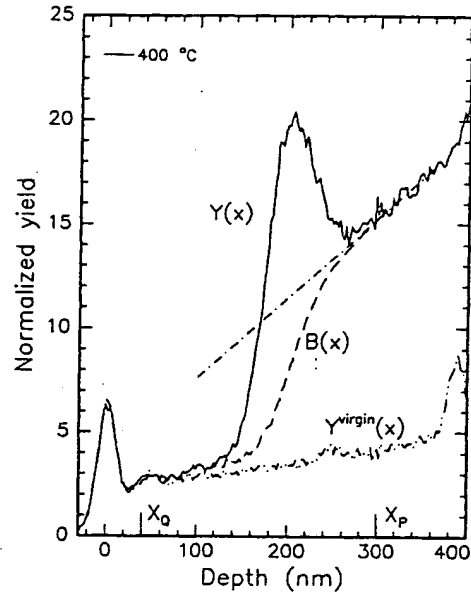The dependence of λ on depth x is specified by the as-

FIG. 13. Procedure for the calculation of the baseline in the RBS spectrum (in principle, x_Q can coincide with the surface, and the baseline is manifestly stable with respect to the choice of x_P provided $x_P \gtrsim 300$ nm).

sumed model of dechanneling. Assuming that there is no additional dechanneling (compared to the undamaged sample) until all of the damaged layer has been crossed by the beam, one has

$$\forall x: \; x_Q \leq x < x_P \Longrightarrow \lambda(x)=0 \qquad (\text{A2})$$

(this choice produces a lower limit to the baseline); taking $\lambda(x)$ such that

$$B(x)= \begin{cases} Y^{\text{unimpl}}(x) & \text{for } 0 < x \leq x_Q \; , \\ Y_Q + (Y_P - Y_Q)(x - x_Q)/(x_P - x_Q) & \text{for } x_Q < x \leq x_P \; , \\ Y(x) & \text{otherwise} \; , \end{cases} \qquad (\text{A3})$$

one encounters the frequently used "linear dechanneling approximation."

We quantitatively specify assumption (A) by assuming

$$\lambda(x) \propto \int_{x_Q}^{x} D(x)dx \; .$$

The constant of proportionality is calculated by specializing this relationship to the endpoint P, where $\lambda(x_P)=1$, so that

$$\lambda(x)= \int_{x_Q}^{x} D(x)dx \Big/ \int_{x_Q}^{x_P} D(x)dx = A \int_{x_Q}^{x} D(x)dx \; ,$$

$$(\text{A4})$$

with

$$A = \left[\int_{x_Q}^{x_P} D(x)dx \right]^{-1} \; .$$

Inserting (A4) into (A1), one gets the following integral equation:

$$B(x)= Y^{\text{unimpl}}(x) \left[1 - A \int_{x_Q}^{x} [Y(x)-B(x)]dx \right]$$
$$+ [Y_P + m(x-x_P)] A \int_{x_Q}^{x} [Y(x)-B(x)]dx$$

which can be solved iteratively starting, for instance, from the lower bound $B_0(x)=Y^{\text{unimpl}}(x)$.

Once the baseline is calculated, the profile of direct backscattering yield is immediately calculated. This

profile is eventually transformed into a concentration profile by "normalization to random," i.e., by assuming that the concentration of backscattering centers is given by

$$C(x) = n_{Si} D(x) / D^{random}(x) , \qquad (A5)$$

where $D^{random}(x)$ is the difference of the random signal (coming from a target where all atoms are displaced) minus the baseline (this assumption is realistic for base-lines appreciably lower than the random signal).

The method hitherto described indeed seems objective, as it does not depend on the points Q and P (while point Q is unequivocally determined from the experimental data, point P is, in principle, arbitrary). While both choices (A2) and (A3) have solutions that depend markedly on the somewhat arbitrary choice of P, the method proposed here is very stable with respect to this choice in a wide depth interval, which makes us confident of the robust physical basis of our computed displacement field.

It must be noted, however, that in Eq. (A5) a factor $O(1)$ is ignored because the backscattering yield of a displaced atom (however large is its displacement) has been assumed to be the same as in a randomly oriented crystal. Moreover, if *two* different displacement fields are present (as, for instance, in the case of hydrogen), two factors, in principle different and both $O(1)$, are ignored.

---

[1]P. Deák, L. C. Snyder, M. Heinrich, C. R. Ortiz, and J. W. Corbett, Physica B **170**, 253 (1991).

[2]P. Deák, L. C. Snyder, and J. W. Corbett, Phys. Rev. B **37**, 6887 (1988).

[3]K. J. Chang and D. J. Chadi, Phys. Rev. Lett. **62**, 937 (1989).

[4]N. M. Johnson, C. Herring, and D. J. Chadi, Phys. Rev. Lett. **56**, 769 (1986).

[5]G. F. Cerofolini and R. Bez, J. Appl. Phys. **61**, 1435 (1987).

[6]C. G. Van de Walle, Y. Bar-Yam, and S. T. Pantelides, Phys. Rev. Lett. **60**, 2761 (1988).

[7]C. G. Van de Walle, P. J. H. Denteneer, Y. Bar-Yam, and S. T. Pantelides, Phys. Rev. B **39**, 10 791 (1989).

[8]R. N. Hall, IEEE Trans. Nucl. Sci. NS-31, 320 (1984).

[9]G. F. Cerofolini and G. Ottaviani, Mater. Sci. Eng. B **4**, 19 (1989).

[10]M. Stutzmann, W. Beyer, L. Tapfer, and C. P. Herrero, Physica B **170**, 240 (1991).

[11]J. B. Boyce and S. E. Ready, Physica B **170**, 305 (1991).

[12]N. M. Johnson, F. A. Ponce, R. A. Street, and R. J. Nemanich, Phys. Rev. B **35**, 4166 (1987).

[13]F. A. Ponce, N. M. Johnson, J. C. Tramontana, and J. Walker, in *Microscopy of Semiconducting Materials*, edited by A. G. Cullis and P. D. Augustus, IOP Conf. Proc. No. 87 (Institute of Physics, Bristol, 1987), p. 49.

[14]S. J. Jeng and G. S. Oehrlein, Appl. Phys. Lett. **50**, 1912 (1987).

[15]S. Romani and J. H. Evans, Nucl. Instrum. Methods B **44**, 313 (1990).

[16]S. J. Jeng, G. S. Oehrlein, and G. J. Scilla, Appl. Phys. Lett. **53**, 1735 (1988).

[17]G. F. Cerofolini, L. Meda, C. Volpones, G. Ottaviani, J. De-Fayette, R. Dierckx, D. Donelli, M. Orlandini, M. Anderle, R. Canteri, C. Claeys, and J. Vanhellemont, Phys. Rev. B **41**, 12 607 (1990).

[18]L. Meda, G. F. Cerofolini, G. Ottaviani, R. Tonini, F. Corni, R. Balboni, M. Anderle, R. Canteri, and R. Dierckx, Physica B **170**, 259 (1991).

[19]A. Bourret, in *Microscopy of Semiconducting Materials*, edited by A. G. Cullis and P. D. Augustus, IOP Conf. Proc. No. 87 (Institute of Physics, Bristol, 1987), p. 39.

[20]L. Meda, G. F. Cerofolini, C. Bresolin, R. Dierckx, D. Donelli, M. Orlandini, M. Anderle, R. Canteri, G. Ottaviani, R. Tonini, C. Claeys, J. Vanhellemont, S. Pizzini and S. Farina, in *Semiconductor Silicon 1990*, edited by G. K. Barraclough, J. Chikawa, and H. R. Huff (The Electrochemical Society, Pennington, NJ, 1990), p. 456.

[21]J. F. Ziegler, TRIM, version 5.3 (1989).

[22]S. Roorda, J. M. Poate, D. C. Jacobson, D. J. Eaglesham, B. S. Dennis, S. Dierker, W. C. Sinke, and F. Spaepen, Solid State Commun. **75**, 197 (1990).

[23]G. F. Cerofolini and L. Meda, *Physical Chemistry of, in and on Silicon* (Springer-Verlag, Berlin, 1989).

[24]G. F. Cerofolini, L. Meda, and C. Volpones, J. Appl. Phys. **63**, 4911 (1988).

[25]E. P. Donovan, F. Spaepen, D. Turnbull, J. M. Poate, and D. C. Jacobson, Appl. Phys. Lett. **42**, 698 (1983); J. Appl. Phys. **57**, 1795 (1985).

[26]J. Keinonen, M. Hautala, E. Rauhala, V. Karttunen, A. Kuronen, J. Räisänen, J. Lahtinen, A. Vehanen, E. Punkka, and P. Hautojärvi, Phys. Rev. B **37**, 8269 (1988).

[27]L. M. Howe, M. H. Rainville, H. K. Haugen, and D. A. Thompson, Nucl. Instrum. Methods **170**, 419 (1980).

[28]J. I. Pankove, J. Appl. Phys. **68**, 6532 (1990).

[29]B. Bech Nielsen, J. Olajos, and H. G. Grimmeiss, Phys. Rev. B **39**, 3330 (1989).

[30]B. Bech Nielsen and H. G. Grimmeiss, Phys. Rev. B **40**, 12 403 (1990).

[31]L. Meda, G. F. Cerofolini, R. Dierckx, G. Mercurio, M. Servidori, F. Cembali, M. Anderle, R. Canteri, G. Ottaviani, C. Claeys, and J. Vanhellemont, Nucl. Instrum. Methods B **39**, 381 (1989).
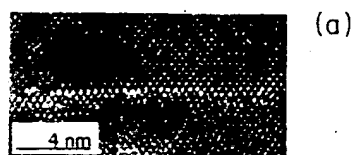
FIG. 7. High-resolution electron micrographs of (a) a {100} platelet, (b) a {111} platelet, and (c) a {113} platelet.
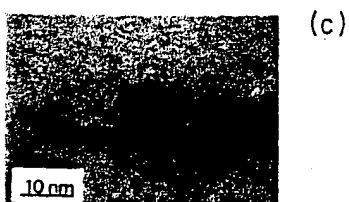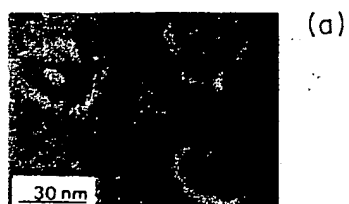
(a)

30 nm

(b)

7 nm

(c)

10 nm

FIG. 8. (a) Near-⟨100⟩-projection plan view of a defective region in a sample annealed at 600 °C for 2 h. Through focal observations in the diffraction-contrast mode have shown that the particles are less dense than the matrix. (b) HREM image of typical defects observed in samples annealed at 600 °C. (c) Near-⟨110⟩-projection cross-sectional view of defects observed in samples annealed at 800 °C. Comparison of (b) and (c) suggests that the defect-growth mechanism is Ostwald ripening.